Structural Disorder in (Bi, M)$_2$(Fe, Mn, Bi)$_2$O$_{6+x}$ (M = Na or K) Pyrochlores Seen from Reverse Monte Carlo Analysis of Neutron Total Scattering

Luke M. Daniels,[1] Helen Y. Playford,[2] Alex C. Hannon[2] and Richard I. Walton[1]*

[1]Department of Chemistry, University of Warwick, Coventry, CV4 7AL, UK;

[2]STFC ISIS Facility, Rutherford Appleton Laboratory, Didcot, Oxford, OX11 0QX, UK;

*To whom correspondence should be addressed: *r.i.walton@warwick.ac.uk*

Abstract

The average structures of the polycrystalline pyrochlores $(Na_{0.60}Bi_{1.40})(Fe_{1.06}Mn_{0.17}Bi_{0.77})O_{6.87}$ and $(K_{0.24}Bi_{1.51})(Fe_{1.07}Mn_{0.15}Bi_{0.78})O_{6.86}$ can be refined through Rietveld refinement against Bragg scattering data using cubic space group $Fd\bar{3}m$, with off-centred 96*h* and 32*e* positions describing the A_2O' network. Investigation of their local structures through neutron total scattering confirms the extent of disorder within these materials, and furthermore shows significant deviation from the average structure, which is not accounted for through analysis of Bragg data alone. Reverse Monte Carlo (RMC) analysis with a 6 × 6 × 6 supercell was used to model accurately this local disorder, revealing ellipsoidal distributions for A-site potassium, distinctly different to the hollow torus-shaped distributions for the sodium and bismuth cations. It is shown through bond valence sum analysis that whilst these atomic displacements allow for the steric preferences of Bi^{3+}, they are also necessary to satisfy the valence of both the bismuth and the alkali metals on the A sites. Analysis of the final RMC configuration showed the BO_6 octahedra for the separate B site metals to be more regular (O–B–O ≈ 90°) than those in the Rietveld model (O–B–O ≈ 85/95°) which describes an average of the three different environments.

Introduction

Oxide pyrochlores $A_2B_2O_6O'$, where the ionic radius of A (eight-coordinate cation) is larger than that of B (six-coordinate cation), typically adopt the cubic symmetry of space group $Fd\bar{3}m$ with the A, B, O and O′ atomic positions commonly defined by the 16*d* (1/2, 1/2, 1/2), 16*c* (0, 0, 0), 48*f* (*x*, 1/8, 1/8), and 8*b* (3/8, 3/8, 3/8) sites, respectively.[1] This apparently simple structure has the ability to accommodate high levels of structural disorder that leads to increased complexity in describing the atomic-scale structure. This disorder can arise from deficiencies of the O′ site or occupancy of this site by other anionic species such as hydroxide or halide ions, metal vacancies on the A site, or the mixing of metals across both the A and B positions, in addition to displacement of any or all of the atoms from their ideal positions.[2] The compositional flexibility of the pyrochlore structure can lead to a wide variety of interesting physical properties and potential applications. Depending upon the metal cations

incorporated, varied electronic behaviour from insulating, through semiconducting, to metallic has been observed,[3-6] as well as low temperature superconductivity.[7-8] Pyrochlores with cation substitutions on both sites, such as $(Bi,Zn)_2(Zn,Nb)_2O_7$ ceramics, have proved useful as dielectric materials.[9-11] Other fields of application for pyrochlores include solid-oxide fuel-cell electrolytes and electrodes,[5, 12] photoluminescence,[13-14] and the immobilisation of radioactive cations from nuclear waste.[15] Extensive study has been undertaken on many pyrochlores due to the phenomenon of frustrated magnetism that results from the geometrical nature of the corner-connected A_4 and B_4 tetrahedral sublattices.[4, 16] Spin glass-like magnetic behaviour has been the focus of attention in many pyrochlores when magnetic ions are included, and has been reported for mixed metal pyrochlores with non-trivial compositions such as $(Bi_{1.89}Fe_{0.11})(Fe_{1.05}Nb_{0.95})O_7$ and $(Bi_{1.88}Fe_{0.12})(Fe_{1.42}Te_{0.58})O_{6.87}$.[17-18]

The use of reverse Monte Carlo (RMC) modelling to interpret pair distribution functions derived from Fourier transformation of total scattering data is becoming increasingly common in the study of disorder in crystalline systems providing local structural information which is usually overlooked in the analysis of Bragg data alone.[19] RMC modelling has been integral to understanding the structural disorder in many stoichiometric and non-stoichiometric pyrochlores; for example, highlighting the presence of coherent Pb^{2+} off-centring, expected for this $6s^2$ 'lone pair' cation, and the correlation of this with low-temperature Einstein modes observed in heat capacity data of the 'ordered-ice' $Pb_2Ru_2O_{6.5}$,[20] as well as understanding order-disorder phenomena in ionic conductor materials by distinguishing the six-coordinate B site and the eight-coordinate A site of the pyrochlore from the nominally seven-coordinate environments of the defect fluorite.[21-22] Another $6s^2$ cation is Bi^{3+} and this is also found in pyrochlore and fluorite oxides where its presence introduces local disorder: for example, in the fast oxide ion conductor δ-Bi_2O_3, the application of RMC showed that the environments local to the Bi^{3+} cations are five-coordinate like those of the α-polymorph, rather than the expected eight-coordinate geometry of the average fluorite structure.[23-24] RMC analysis was used to model cation off-centring in insulating $Bi_2Ti_2O_6O'$, driven by valence requirements, and highlighted the presence of smaller cation displacements in metallic $Bi_2Ru_2O_6O'$ due to screening by conduction electrons of the B site metal.[25] For the ferroelectric perovskite $Na_{0.5}Bi_{0.5}TiO_3$, RMC analysis proved that the environments local to bismuth and sodium are distinct, with each cation showing different displacements away from the ideal A site position.[26-27]

In this paper we describe a neutron total scattering study of two highly disordered pyrochlores, $(Na_{0.60}Bi_{1.40})(Fe_{1.06}Mn_{0.17}Bi_{0.77})O_{6.87}$ and $(K_{0.24}Bi_{1.51})(Fe_{1.07}Mn_{0.15}Bi_{0.78})O_{6.86}$, synthesised through hydrothermal methods. The local disorder present in these materials is accurately modelled by RMC methods and is compared against the average structural models obtained from Rietveld refinement of Bragg data, which we have previously reported.[28] The previous Rietveld refinements reported on the average structures of $(Na_{0.60}Bi_{1.40})(Fe_{1.06}Mn_{0.17}Bi_{0.77})O_{6.87}$ and $(K_{0.24}Bi_{1.51})(Fe_{1.07}Mn_{0.15}Bi_{0.78})O_{6.86}$ pyrochlores presented strong evidence for complex disorder, as might be expected with the multiple occupancy of both the A and B sites and presence of stereochemically-active lone-pair cation Bi^{3+}, resulting in increased metal off-centring and distortion of the local oxygen environment.[28] This prompted a more detailed examination of the structures of these materials, using the same dataset as previously measured,[27] but now making use of the high momentum transfer range for PDF analysis.

Experimental Methods

The hydrothermal syntheses of the two pyrochlores was performed as reported previously,[28] with sodium bismuthate(V) dihydrate (0.5 g; 85% Acros Organics), iron(III) nitrate nonahydrate (0.3306 g; 98% Aldrich) and manganese(II) nitrate tetrahydrate (0.0313 g; 99% Alfa Aesar) dissolved into solutions of either sodium or potassium hydroxide (4.0 M) before being heated in sealed stainless-steel autoclaves to 200 °C for six hours.

Neutron total scattering data were collected using the GEneral Materials diffractometer (GEM) at ISIS, the U.K. spallation neutron source.[29] The dried, powdered samples were loaded into thin-walled vanadium cylindrical cans of inner diameter 0.6 cm and wall thickness of 0.004 cm. The effect of incoherent scatter by hydrogen was minimised by synthesising all powders in D_2O, whilst residual moisture was removed by drying at 80 °C overnight under reduced pressure in a ThermoScientific Heraeus Kelvitron T vacuum oven prior to measurement. To achieve a high statistical quality, data were recorded for six hours from each sample. Data were also collected from an empty vanadium can, the empty instrument, and a vanadium rod of 0.834 cm diameter for normalisation purposes.

Data from four different detector banks on GEM (banks 2 - 5) were merged to produce the distinct scattering, i(Q), in the program GudrunN (Figure 1a).[30] Fourier transformation of

i(Q) using Q_{max} of 26 Å^{-1} and the step modification function, M(Q), yields the differential correlation function, D(r), also known as the pair distribution function (PDF), shown through Equation 1 (Figure 1b).

$$\mathrm{D}(r) = \frac{2}{\pi}\int_0^{Q_{max}} Qi(Q)\mathrm{M}(Q)\sin(rQ)\mathrm{d}Q \quad (1)$$

Refinements of the structural models obtained from Rietveld analysis against the PDF data were performed using the program PDFgui.[31]

The total correlation function, T(r), relates to the PDF through Equation 2,

$$\mathrm{T}(r) = 4\pi r g^0\left(\sum_l c_l\bar{b}_l\right)^2 + \frac{2}{\pi}\int_0^{Q_{max}} Qi(Q)M(Q)\sin(rQ)\mathrm{d}Q \quad (2)$$

where g^0 is the atomic number density, and c_l and $\bar{b}_l$ are the atomic fraction and coherent scattering length for element l, respectively.[29] Analyses of the first and second correlations in the T(r) were undertaken through a peak fitting approach. The fitting of a resolution-broadened Gaussian to the first (or first few) correlations to obtain its area is a commonly-used method in the study of non-crystalline materials like glasses and liquids.[29, 32] In this instance, it was used to model the first two correlations in the T(r) based on contributions from the individual B site metals and oxide ions by using the distance between atoms l and l', $r_{ll'}$, and coordination number of the central atom (l) from bond valence in Equation 3,

$$n_{ll'} = \frac{r_{ll'}A_{ll'}}{(2-\delta_{ll'})c_l\bar{b}_l\bar{b}_{l'}} \quad (3)$$

where $A_{ll'}$ is the area of the peak and $\delta_{ll'}$ is the Kronecker delta.[33]

The program RMCProfile was used for reverse Monte Carlo modelling of the PDF data.[34] The datasets used for RMC were the Bragg scattering data from bank 3 of GEM and the pair distribution function, D(r). Correlations in the D(r) below r = 1.76 Å were determined to be nonphysical by displaying a dependence upon the value of Q_{max}, and were therefore excluded from the RMC fit.

Results and Discussion

The crystallographic disorder revealed previously by Rietveld refinement of $(Na_{0.60}Bi_{1.40})(Fe_{1.06}Mn_{0.17}Bi_{0.77})O_{6.87}$ and $(K_{0.24}Bi_{1.51})(Fe_{1.07}Mn_{0.15}Bi_{0.78})O_{6.86}$ pyrochlores (henceforth referred to as Na- and K-pyrochlore, respectively) was accounted for by off-

centre A and O′ positions modelled using the 96*h* and 32*e* positions in the $Fd\bar{3}m$ space group,[28] respectively (Supporting Information, Figure S1), commonly used to account for disorder in pyrochlores when analysis of Bragg scattering is performed.[18, 35-39] The incorporation of multiple metals on both the A and B sites, and the mixing of bismuth across both cation sites add further complexity to the complete description of the structures of our materials. The PDFs derived from both pyrochlores indicate that their structures are very similar (Figure 1), displaying sharp, resolved features out to distances well beyond 25 Å, showing that the extended structure of these materials resembles a crystalline pyrochlore, consistent with our previous analysis and implying that disorder is present only on a local length scale. The shortest interatomic correlation observed in the PDFs of both pyrochlores corresponds to contributions from the B–O distances between the octahedral B site metal and coordinating 48*f* oxygen, agreeing well with the expected distance of ~2.06 Å from the Rietveld model. The second, much broader, correlation consists of contributions from both the A–O and non-bonding O–O distances. In an ideal stoichiometric pyrochlore, with the A site metals on the 16*d* position, the neighbouring oxide positions are situated 2.33-2.4 Å from the cations, however, with the displacement of the A site away from the ideal position, in reality the range of A–O bond lengths in these two materials is expected to be much larger, with potential distances over 2.3-2.9 Å.

Figure 2a and 2b display fits to the PDFs of both pyrochlores using the Rietveld model as a starting point and with refinement of the coordinates of the 96*h* and 48*f*(*x*) atomic positions, and atomic displacement parameters (Supporting Information, Table S1). It is clear that the Rietveld model provides a good description of the mid-to-long range structure over length scales larger than the unit cell, however, for the low *r* region ($r < 5$ Å), the fit is rather poor implying that the average model does not account for the local structure present in these pyrochlores even when using the displaced 96*h* and 32*e* positions. Confining the A site cations on the 16*d* site and O′ site onto the 8*b* position results in a poorer fit than either of the above (Supporting information, Figure S2). It is of particular note that the main discrepancies between the data and model arise from the second and third pair correlations at $r = 2.9$ and 3.75 Å, respectively, involving the A and O′ sites, whose local coordination environments are likely to be complex, given the presence of the lone pair cation Bi^{3+}. Although the areas of the first and fourth peaks are not accurately reproduced, their simulated positions are modelled well indicating that the bond distances responsible for these correlations are correct. Fitting only the low *r* region of the PDF improved the modelled areas of these peaks over

fitting to 20 Å, highlighting further the inconsistencies between the short-range and average long-range structures. The fit to the low *r* region can be enhanced through relaxation of the $Fd\bar{3}m$ symmetry using the non-centrosymmetric subgroup $F\bar{4}3m$ (Figure 2c and 2d). This provides a convenient means of creating a lower symmetry model for small-box modelling; by removing the centrosymmetric constraint it can allow the structure some flexibility to fit the local structure whilst maintaining the average cubic symmetry observed through Rietveld analysis,[28] without introducing too many parameters to the refinement. This has been used to model successfully the short-range disorder in a range of metal oxides that have average long-range structures based upon $Fd\bar{3}m$ symmetry,[40-41] and in particular accurately describes the structures of many pyrochlore materials.[42-48] More recently, a symmetry-based approach showed how a monoclinic cell was required to model correctly the much-debated α-structure of pyrochlore $Bi_2Sn_2O_7$.[32] However, for our materials we find no evidence in the diffraction data for such superstructures (extra weak Bragg peaks in the data are due only to a small level of α-Bi_2O_3 impurity, which has negligible contribution to the total PDF, Supporting Information Figure S3) and the simulated PDFs using these symmetries show similar discrepancies as those modelled from $Fd\bar{3}m$, with significant deviation observed on the local scale for the second and third atomic pair correlations (Supporting Information, Figure S4). Through peak fitting, it is possible to model the first peak of the PDF using the separate contributions from the three metals on the B site (Figure 3a). The Rietveld model constrains the three metals to the same position, leading to identical distances to the neighbouring 48*f* oxide anions for each metal, 2.0651 and 2.0635 Å for the Na- and K-pyrochlores, respectively. In reality, the metals have different ionic radii, and therefore would not share the same distance with the neighbouring oxygen positions (Supporting Information, Table S2). Rietveld refinement thus results in an average of the three different environments, which is a possible explanation of why the refined *x* positional parameter for the 48*f* oxide position in both pyrochlores has a value above 0.3125 (x = 0.32770(7) for Na-pyrochlore, x = 0.32704(6) for K-pyrochlore), which corresponds to regular symmetric BO_6 octahedra. This simple modelling of the second correlation in the PDF is more difficult due to contributions from several atom pairs such as A–O and O–O (Figure 3b), however, it is worth noting that modelling three separate B–O distances would therefore result in three sizes of BO_6 octahedra, each with different distances between their vertex oxide ions. Using three separate O–O distances for each B site metal improves the fit to the second correlation in the PDF (Figure 3c), with the contributions of each being weighted by the metal occupancy and

neutron scattering length. Despite the A site accommodating the majority of the disorder, the disorder resulting from metal mixing on the B site must also be considered in order to achieve a true model of the short-range structure in these materials.

To avoid the limitations inherent in crystallographic analysis of Bragg diffraction data, a large configuration of atoms, built from Rietveld models with the atoms on the ideal sites (16*d*, 16*c*, 48*f* and 8*b*) was analysed through the reverse Monte Carlo (RMC) method.[34] A 6 × 6 × 6 supercell was generated from the Rietveld models for each pyrochlore, leading to configurations built from 216 unit cells containing a total of 19008 atoms. A larger 8 × 8 × 8 supercell was also tested but no improvement in the final fit was achieved and the increased number of atoms (45056) resulted in the calculations becoming significantly more computationally expensive. The oxygen vacancies for each pyrochlore, and the A site vacancies of the K-pyrochlore were distributed randomly within the configurations, and an atom-swap procedure was used to randomise the configuration such that initial bias was minimised in the fitting.[34] Bond valence sum (BVS) constraints and hard-sphere cut-off distances were defined for each ion present in the configuration to maintain physically reasonable coordination environments.[49] The BVS weightings were set to be the same for each cation, while weightings for both the O and O′ positions were higher (relative weightings for cations and anions were 0.01 and 0.02, respectively). To ensure that the resulting configurations agree with both the short-range structure and long-range periodicity, fits were made simultaneously against both the real-space D(*r*), and also reciprocal-space Bragg data from bank 3 of GEM. Figure 4 shows fits against these data after approximately eight million random atom moves were generated and tested, and no further improvements were observed. The figures show that excellent agreements between model and data in the low *r* region of the PDFs (Figures 4a and 4b) are possible through RMC whilst maintaining a satisfactory fit to the Bragg data (Figures 4c and 4d). The intensities of Bragg reflections are correctly modelled and the fits are comparable to those obtained through Rietveld refinement, showing that the atoms need to be displaced only slightly away from crystallographic positions such that the fit to the average structure is not degraded and the disorder described by the PDF is simultaneously modelled.

The RMC configurations were built from models based on the ideal $Fd\bar{3}m$ cubic pyrochlore with the A sites on the 16*d* positions, and O′ sites on the 8*b* positions, so it is interesting that refinement of the configurations always resulted in these two particular sites moving away from the ideal position, much like in their Rietveld models (Figures 5a and 5b and 5c). Close

inspection reveals well-defined, compact B site atom "clouds", despite the presence of three different B site metals. (Supporting Information, Figure S6) and therefore that the majority of the disorder in these pyrochlores resides on the A_2O' network. The O' 8*b* sites display the most largest "clouds", consistent with the Rietveld models where large displacement parameters were required to model accurately these positions. Throughout the RMC refinements, the A site metals are observed to move away from their central positions forming anisotropic distributions that are elongated within the plane of the neighbouring 48*f* oxygen atoms (Figure 5d). When viewing the A sites of the RMC configurations along the [111] direction, normal to the O′–Bi–O′ distances, it becomes clear that they have been sufficiently displaced from their average crystallographic site to form torus-shaped distributions, where atom density is greater at the edges of these distributions rather than the centre (Figure 5e and 5f), and thus resembling the 96*h* sites of the Rietveld model. The displacements for the A site cations are comparable to those of ≈ 0.3285 Å from Rietveld refinement (Figure 6a and 6b), however, through RMC it is clear that the separate metals are all displaced by different amounts from the ideal position (Bi^{3+} displacement in both pyrochlores ≈0.4 Å, Na^+ displacement ≈0.425 Å, K^+ displacement ≈0.35 Å). Furthermore, the Bi^{3+} distributions show suggestions of six-fold symmetry to the tori (Figure 5e and 5f) corresponding to that of the 96*h* position, with the corners of the hexagon directed in between the neighbouring 48*f* positions. Similar displacements of ≈0.4 Å were observed for the A site in an RMC study of $Bi_2Ti_2O_7$ for which Bi^{3+} was also found to be displaced off-centre from its ideal position in hollow rings with the O′ sites distributed in a tetrapod centred around the ideal site.[50] It was concluded in that study that these displacements resulted from the need to satisfy Bi^{3+} valence with the surrounding (48*f*) oxygen and allowed the lone pair to be accommodated in the opposite direction, which resulted in zig-zag arrangements of neighbouring bismuth atoms. A study of $Bi_2Ru_2O_7$, however, exhibited incoherent atom displacements of much smaller magnitude as these were driven solely by lone pair effects.[25] It is also interesting to note that alongside their different displacement magnitudes, differences in the distributions of the separate A site metals in $(Na_{0.60}Bi_{1.40})(Fe_{1.06}Mn_{0.17}Bi_{0.77})O_{6.87}$ and $(K_{0.24}Bi_{1.51})(Fe_{1.07}Mn_{0.15}Bi_{0.78})O_{6.86}$ are revealed through RMC analysis (Figure 6c and 6d). The distributions of Bi^{3+} in both pyrochlores show that the highest density is focused around average displacement distances of ≈0.4 Å, supporting the hollow torus-shaped distributions with little to no density in the centre observed in Figure 5. Interestingly, the distributions of the alkali metals are not the same; sodium is distributed similarly to the bismuth with low density in the centre of a "hollow"

ring, whereas potassium is uniformly flattened into ellipsoids within the plane of the neighbouring 48*f* oxide ions, normal to the disordered O′ sites. The different distributions of alkali metals are likely due to the valence requirements of each; potassium is much larger than sodium (K^+ ionic radius = 1.51 Å, Na^+ ionic radius = 1.18 Å, based on eight-coordinate values), and as a result smaller displacements are needed to satisfy the valence requirements of potassium, compared to sodium. This shows that bismuth and alkali metals occupying the same average crystallographic position need to modelled separately, a distinction that may prove important to many materials and indeed was observed previously in $Na_{0.5}Bi_{0.5}TiO_3$ ferroelectrics.[26-27]

The partial contributions to the PDFs from RMC modelling of each pyrochlore (Figure 7a and 7b) highlight the contributions to the first few peaks of the PDF. As expected from the Rietveld model and the peak fitting approach implemented in Figure 3, the main contributions to the first correlation (~2.06 Å) are from distances involving the B site metals and the coordinating 48*f* oxide ions in the BO_6 octahedra. Interestingly, the A site metals are displaced sufficiently that distances involving these atoms also contribute to the first correlation. Contributions over a broad range of distances from 2.1-3.0 Å are observed for correlations between bismuth and oxygen, including both the O and O′ positions. This is also the case for sodium, whereas potassium-oxygen distances cover a shorter range of 2.35-3.0 Å. The main contribution to the second correlation comes from the shortest non-bonding oxygen-oxygen distances, involving the 48*f* oxide ions on the vertices of the BO_6 octahedra. This again supports the fits to the PDF shown in Figure 3c and highlights the broad range of distances that these O–O correlations can cover when multiple metals are incorporated onto the octahedral position. As a result of the B site metals being modelled in accordance with their different valence requirements, the octahedra for each are more regular than those described by the average Rietveld models, with O–B–O bond angle distributions centred around ≈90°, Figure 7c. Although the octahedra are more regular, the multiple O–O correlations lead to increased disorder in the 48*f* oxygen positions, which was accounted for in the Rietveld refinements by distortion of the octahedra such that angles adopted the discrete values of 85 and 95°. The bond valence sums of the metals present in these models are summarised in Table 1, alongside the values from the Rietveld models, which are clearly erroneous. The metals modelled on the same crystallographic position are distinguished in the refined RMC configurations with clear evidence of A and B site bismuth in +3 and +5 oxidation states, respectively, and also the three separate B site metals, supporting the

experimental results from XANES analysis reported previously.[28] The final bond valence distributions for both pyrochlores are shown in Figure 8 and are compared against those from Rietveld refinement. Also shown are distributions from RMC configurations refined without BV constraints. It is clear that to guide the simulations toward accurate end models these BV constraints are required to maintain chemical sense, and it shows that the displacements observed in Figure 5 and Figure 6 are not driven solely by the steric requirements of Bi^{3+}, but are also necessary to maintain physical valence sums for the cations, as observed previously in $Bi_2Ti_2O_7$.[25]

Conclusions

Investigations using neutron total scattering have shown how on a local scale the structures of the two pyrochlores, $(Na_{0.60}Bi_{1.40})(Fe_{1.06}Mn_{0.17}Bi_{0.77})O_{6.87}$ and $(K_{0.24}Bi_{1.51})(Fe_{1.07}Mn_{0.15}Bi_{0.78})O_{6.86}$, deviate from the average $Fd\bar{3}m$ models obtained previously from Rietveld analysis, in which the A and O′ sites were displaced from their ideal positions to attain best agreement between data and model. Attempts using lower symmetry variants of the average Rietveld structure were made, however, a true description of the local disorder present in these materials required that the symmetry constraints of crystallography be removed. Further information about the local coordination of metals within these materials was revealed by modelling accurately the short-range structure using a reverse Monte Carlo approach, whilst agreeing with the average periodic structure through simultaneous fitting of Bragg data. Atomic probability densities showed the formation of hollow tori of sodium and bismuth and flattened ellipsoids of potassium within the plane of the surrounding 48*f* oxygen anions, normal to the O′–A–O′ chain, with diffuse clouds representing the O′ 8*b* sites. RMC modelling demonstrated that the observed off-centring is not driven solely by steric requirements of the lone pair Bi^{3+} cation, with both alkali metals also being displaced, which is necessary to stabilise the valence of the metals present. RMC analysis showed that the three different metals on the B site each have more regular local octahedral environments than the Rietveld models showed and lead to further disorder in the 48*f* oxygen sites which share bonding with the off-centred A site cations; information which is lost within large thermal displacement parameters through analysis of Bragg data alone. While this is not the first time that such conclusions have been drawn from this type of study, it highlights how analysis of all of the information contained within a diffraction pattern through total scattering methods is necessary to understand fully the structures of complex materials, and

for the analysis of mixed-metal pyrochlores provides an approach to modelling their structures that will be applicable to other compositions.

Acknowledgements

We thank the EPSRC (EP/J500586) and the STFC Centre for Materials Physics and Chemistry for co-funding the studentship of LMD (CMPC11104). Some of the instruments used at the University of Warwick were obtained through the Science City Advanced Materials project "Creating and Characterising Next Generation Advanced Materials" with support from Advantage West Midlands (AWM) and part funded by the European Regional Development Fund (ERDF). We acknowledge STFC for the provision of neutron beamtime and for computing resources provided by STFC Scientific Computing Department's SCARF cluster.

Supporting Information for Publication:

Further details on the Rietveld models, fitting PDF data with various pyrochlore A and O′ sites, the peak fitting approach, comparison of $T^0(r)$ slopes against density and composition, and comparison of the Rietveld structure against RMC supercells are provided. This material is available free of charge via the Internet at http://pubs.acs.org. The research data supporting this publication can be accessed at: http://wrap.warwick.ac.uk/90401/

Tables

Table 1: Comparison of bond valence sums for both pyrochlores from Rietveld refinement to those refined from RMC configurations with and without bond valence constraints.

Element (ideal site)	Rietveld BVS	RMC [6×6×6] box	RMC without BV
Na-pyrochlore			
Bi^{3+} (A - 16*d*)	2.61	2.83	2.35
Na^{+} (A - 16*d*)	1.19	1.00	1.16
Fe^{3+} (B - 16*c*)	2.62	2.94	2.71
Mn^{4+} (B - 16*c*)	2.58	3.79	2.63
Bi^{5+} (B - 16*c*)	5.93	5.10	6.10
O^{2-} (O - 48*f*)	1.74	1.72	1.70
O^{2-} (O′ - 8*b*)	1.82	2.23	2.08
K-pyrochlore			
Bi^{3+} (A - 16*d*)	2.44	2.85	2.39
K^{+} (A - 16*d*)	2.88	1.03	2.66
Fe^{3+} (B - 16*c*)	2.63	2.91	2.63
Mn^{4+} (B - 16*c*)	2.58	3.85	2.81
Bi^{5+} (B - 16*c*)	5.94	5.08	5.97
O^{2-} (O - 48*f*)	1.87	1.71	1.68
O^{2-} (O′ - 8*b*)	1.89	2.29	2.39

References

1. Subramanian, M. A.; Aravamudan, G.; Subba Rao, G. V., Oxide Pyrochlores - A Review. *Prog. Solid St. Chem.* **1983**, *15*, 55-143.
2. Modeshia, D. R.; Walton, R. I., Solvothermal Synthesis of Perovskites and Pyrochlores: Crystallisation of Functional Oxides Under Mild Conditions. *Chem. Soc. Rev.* **2010**, *39*, 4303-4325.
3. Fujimoto, S., Geometrical-Frustration-Induced (Semi)Metal-to-Insulator Transition. *Phys. Rev. Lett.* **2002**, *89*, 226402.
4. Gaultois, M. W.; Barton, P. T.; Birkel, C. S.; Misch, L. M.; Rodriguez, E. E.; Stucky, G. D.; Seshadri, R., Structural Disorder, Magnetism, and Electrical and Thermoelectric Properties of Pyrochlore $Nd_2Ru_2O_7$. *J. Phys.: Condens. Matter* **2013**, *25*, 186004.
5. Weller, M. T.; Hughes, R. W.; Rooke, J.; Knee, C. S.; Reading, J., The Pyrochlore Family - Potential Panacea for the Frustrated Perovskite Chemist. *Dalton Trans.* **2004**, *19*, 3032-3041.
6. Yamaura, J.; Ohgushi, K.; Ohsumi, H.; Hasegawa, T.; Yamauchi, I.; Sugimoto, K.; Takeshita, S.; Tokuda, A.; Takata, M.; Udagawa, M.; et al., Tetrahedral Magnetic Order and the Metal-Insulator Transition in the Pyrochlore Lattice of $Cd_2Os_2O_7$. *Phys. Rev. Lett.* **2012**, *108*, 247205.
7. Kasahara, Y.; Shimono, Y.; Shibauchi, T.; Matsuda, Y.; Yonezawa, S.; Muraoka, Y.; Hiroi, Z., Thermal Conductivity of the Pyrochlore Superconductor KOs_2O_6: Strong Electron Correlations and Fully Gapped Superconductivity. *Phys. Rev. Lett.* **2006**, *96*, 247004.
8. Sakai, H.; Yoshimura, K.; Ohno, H.; Kato, H.; Kambe, S.; Walstedt, R. E.; Matsuda, T. D.; Haga, Y.; Onuki, Y., Superconductivity in a Pyrochlore Oxide, $Cd_2Re_2O_7$. *J. Phys.: Condens. Matter* **2001**, *13*, 785-790.
9. Krayzman, V.; Levin, I.; Woicik, J. C., Local Structure of Displacively Disordered Pyrochlore Dielectrics. *Chem. Mater.* **2007**, *19*, 932-936.
10. Liu, Y.; Withers, R. L.; Welberry, T. R.; Wang, H.; Du, H.-L.; Yao, X., Structural Disorder in BZN-Based Pyrochlores. *J. Electroceram.* **2007**, *21*, 401-404.
11. Withers, R. L.; Welberry, T. R.; Larsson, A. K.; Liu, Y.; Norén, L.; Rundlöf, H.; Brink, F. J., Local Crystal Chemistry, Induced Strain and Short Range Order in the Cubic Pyrochlore $(Bi_{1.5-\alpha}Zn_{0.5-\beta})(Zn_{0.5-\gamma}Nb_{1.5-\delta})O_{(7-1.5\alpha-\beta-\gamma-2.5\delta)}$ (BZN). *J. Solid State Chem.* **2004**, *177*, 231-244.
12. Lian, J.; Wang, L. M.; Wang, S. X.; Chen, J.; Boatner, L. A.; Ewing, R. C., Nanoscale Manipulation of Pyrochlore: New Nanocomposite Ionic Conductors. *Phys. Rev. Lett.* **2001**, *87*, 145901.
13. Jin, D.; Yu, X.; Yang, H.; Zhu, H.; Wang, L.; Zheng, Y., Hydrothermal Synthesis and Luminescence Properties of Yb^{3+} Doped Rare Earth Stannates. *J. Alloys Compd.* **2009**, *474*, 557-560.
14. Nyman, M.; Rodriguez, M. A.; Shea-Rower, L. E.; Martin, J. E.; Provencio, P. P., Highly Versatile Rare Earth Tantalate Pyrochlore Nanophosphors. *J. Am. Chem. Soc.* **2009**, *131*, 11652-11653.
15. Zhang, F. X.; Lang, M.; Liu, Z.; Ewing, R. C., Pressure-Induced Disordering and Anomalous Lattice Expansion in $La_2Zr_2O_7$ Pyrochlore. *Phys. Rev. Lett.* **2010**, *105*, 015503.
16. Gardner, J. S.; Gingras, M. J. P.; Greedan, J. E., Magnetic Pyrochlore Oxides. *Rev. Mod. Phys.* **2010**, *82*, 53-107.
17. Babu, G. S.; Bedanta, S.; Valant, M., Evidence of the Spin Glass State in $(Bi_{1.88}Fe_{0.12})(Fe_{1.42}Te_{0.58})O_{6.87}$ Pyrochlore. *Solid State Commun.* **2013**, *158*, 51-53.
18. Miiller, W.; Causeret, L.; Ling, C. D., Frustrated Magnetism and Local Structural Disorder in Pyrochlore-Type $Bi_{1.89}Fe_{1.16}Nb_{0.95}O_{6.95}$. *J. Phys.: Condens. Matter* **2010**, *22*, 486004.
19. Playford, H. Y.; Owen, L. R.; Levin, I.; Tucker, M. G., New Insights into Complex Materials Using Reverse Monte Carlo Modeling. *Annu. Rev. Mater. Res.* **2014**, *44*, 429-449.
20. Shoemaker, D. P.; Llobet, A.; Tachibana, M.; Seshadri, R., Reverse Monte Carlo Neutron Scattering Study of the 'Ordered-Ice' Oxide Pyrochlore $Pb_2Ru_2O_{6.5}$. *J. Phys.: Condens. Matter* **2011**, *23*, 315404.

21. Norberg, S. T.; Hull, S.; Eriksson, S. G.; Ahmed, I.; Kinyanjui, F.; Biendicho, J. J., Pyrochlore to Fluorite Transition: The $Y_2(Ti_{1-x}Zr_x)_2O_7$ ($0.0 \le x \le 1.0$) System. *Chem. Mater.* **2012**, *24*, 4294-4300.
22. Payne, J. L.; Tucker, M. G.; Evans, I. R., From Fluorite to Pyrochlore: Characterisation of Local and Average Structure of Neodymium Zirconate, $Nd_2Zr_2O_7$. *J. Solid State Chem.* **2013**, *205*, 29-34.
23. Hull, S.; Norberg, S. T.; Tucker, M. G.; Eriksson, S. G.; Mohn, C. E.; Stolen, S., Neutron Total Scattering Study of the δ and β Phases of Bi_2O_3. *Dalton Trans.* **2009**, 8737-8745.
24. Norberg, S. T.; Eriksson, S. G.; Hull, S., Comparison of Short-Range Ion–Ion Correlations in the α, β and δ Phases of Bi_2O_3. *Solid State Ionics* **2011**, *192*, 409-412.
25. Shoemaker, D. P.; Seshadri, R.; Tachibana, M.; Hector, A. L., Incoherent Bi Off-Centering in $Bi_2Ti_2O_6O'$and $Bi_2Ru_2O_6O'$: Insulator Versus Metal. *Phys. Rev. B* **2011**, *84*, 064117.
26. Jeong, I.; Park, C. Y.; Kim, D. J.; Kim, S.-h.; Moon, B. K.; Kim, I. W.; Ahn, C. W., Neutron Total Scattering Studies on A-Site Disorder in Lead-Free Ferroelectric $Bi_{0.5}(Na_{1-x}K_x)_{0.5}TiO_3$. *Z. Kristallogr.* **2011**, *226*, 150-154.
27. Keeble, D. S.; Barney, E. R.; Keen, D. A.; Tucker, M. G.; Kreisel, J.; Thomas, P. A., Bifurcated Polarization Rotation in Bismuth-Based Piezoelectrics. *Adv. Funct. Mater.* **2013**, *23*, 185-190.
28. Daniels, L. M.; Playford, H. Y.; Greneche, J. M.; Hannon, A. C.; Walton, R. I., Metastable (Bi, *M*)$_2$(Fe, Mn, Bi)$_2O_{6+x}$ (*M* = Na or K) Pyrochlores from Hydrothermal Synthesis. *Inorg. Chem.* **2014**, *53*, 13197-13206.
29. Hannon, A. C., Results on Disordered Materials from the GEneral Materials Diffractometer, GEM, at ISIS. *Nucl. Instrum. Methods Phys. Res., Sect. A* **2005**, *551*, 88-107.
30. Soper, A. K. *Rutherford Appleton Laboratory Technical Report RAL-TR-2011-013*; 2011.
31. Farrow, C. L.; Juhas, P.; Liu, J. W.; Bryndin, D.; Bozin, E. S.; Bloch, J.; Proffen, T.; Billinge, S. J., PDFfit2 and PDFgui: Computer Programs for Studying Nanostructure in Crystals. *J. Phys.: Condens. Matter* **2007**, *19*, 335219.
32. Lewis, J. W.; Payne, J. L.; Evans, I. R.; Stokes, H. T.; Campbell, B. J.; Evans, J. S., An Exhaustive Symmetry Approach to Structure Determination: Phase Transitions in $Bi_2Sn_2O_7$. *J. Am. Chem. Soc.* **2016**, *138*, 8031-8042.
33. Brese, N. E.; O'Keeffe, M., Bond-Valence Parameters for Solids. *Acta Cryst. B* **1991**, *47*, 192-197.
34. Tucker, M. G.; Keen, D. A.; Dove, M. T.; Goodwin, A. L.; Hui, Q., RMCProfile: Reverse Monte Carlo for Polycrystalline Materials. *J. Phys.: Condens. Matter* **2007**, *19*, 335218.
35. Henderson, S. J.; Shebanova, O.; Hector, A. L.; McMillan, P. F.; Weller, M. T., Structural Variations in Pyrochlore-Structured $Bi_2Hf_2O_7$, $Bi_2Ti_2O_7$ and $Bi_2Hf_{2-x}Ti_xO_7$ Solid Solutions. *Chem. Mater.* **2007**, *19*, 1712-1722.
36. Lufaso, M. W.; Vanderah, T. A.; Pazos, I. M.; Levin, I.; Roth, R. S.; Nino, J. C.; Provenzano, V.; Schenck, P. K., Phase Formation, Crystal Chemistry, and Properties in the System Bi_2O_3–Fe_2O_3–Nb_2O_5. *J. Solid State Chem.* **2006**, *179*, 3900-3910.
37. Nguyen, H. B.; Norén, L.; Liu, Y.; Withers, R. L.; Wei, X.; Elcombe, M. M., The Disordered Structures and Low Temperature Dielectric Relaxation Properties of Two Misplaced-Displacive Cubic Pyrochlores Found in the Bi_2O_3–$M^{II}O$–Nb_2O_5 (*M*=Mg, Ni) Systems. *J. Solid State Chem.* **2007**, *180*, 2558-2565.
38. Vanderah, T. A.; Siegrist, T.; Lufaso, M. W.; Yeager, M. C.; Roth, R. S.; Nino, J. C.; Yates, S., Phase Formation and Properties in the System Bi_2O_3:$2CoO_{1+x}$:Nb_2O_5. *Eur. J. Inorg. Chem.* **2006**, *2006*, 4908-4914.
39. Zhou, Q.; Kennedy, B. J.; Ting, V.; Withers, R. L., Thermal Expansion and Cation Disorder in Bi_2InNbO_7. *J. Solid State Chem.* **2005**, *178*, 1575-1579.
40. Playford, H. Y.; Hannon, A. C.; Barney, E. R.; Walton, R. I., Structures of Uncharacterised Polymorphs of Gallium Oxide from Total Neutron Diffraction. *Chem. - Eur. J.* **2013**, *19*, 2803-2813.
41. Playford, H. Y.; Hannon, A. C.; Tucker, M. G.; Lees, M. R.; Walton, R. I., Total Neutron Scattering Investigation of the Structure of a Cobalt Gallium Oxide Spinel Prepared by Solvothermal Oxidation of Gallium Metal. *J. Phys.: Condens. Matter* **2013**, *25*, 454212.

42. Alonso, J. A.; Cascales, C.; Rasines, I.; Pannetier, J., Oxygen Vacancy Ordering in the Defect Pyrochlore $Pb_2[TiSb]O_{6.5}$: A Rietveld Refinement of Neutron Powder Diffraction Data. *Acta Cryst. C* **1989**, *45*, 3-7.

43. Beyerlein, R. A.; Horowitz, H. S.; Longo, J. M.; Leonowicz, M. E., Neutron Diffraction Investigation of Ordered Oxygen Vacancies in the Defect Pyrochlores, $Pb_2Ru_2O_{6.5}$ and $PbTiNb_2O_{6.5}$. *J. Solid State Chem.* **1984**, *51*, 253-265.

44. Fukina, D. G.; Suleimanov, E. V.; Yavetskiy, R. P.; Fukin, G. K.; Boryakov, A. V.; Borisov, E. N.; Borisov, E. V.; Surodin, S. I.; Saharov, N. V., Single Crystal Structure and SHG of Defect Pyrochlores $CsBVMoO_6$ (BV=Nb,Ta). *J. Solid State Chem.* **2016**, *241*, 64-69.

45. Hanawa, M.; Yamaura, J.; Muraoka, Y.; Sakai, H.; Hiroi, Z., Structural Phase Transition in the Superconducting Pyrochlore Oxide $Cd_2Re_2O_7$. *J. Phys. Chem. Solids* **2002**, *63*, 1027-1030.

46. Playford, H. Y.; Modeshia, D. R.; Barney, E. R.; Hannon, A. C.; Wright, C. S.; Fisher, J. M.; Amieiro-Fonseca, A.; Thompsett, D.; O'Dell, L. A.; Rees, G. J.; et al., Structural Characterization and Redox Catalytic Properties of Cerium(IV) Pyrochlore Oxides. *Chem. Mater.* **2011**, *23*, 5464-5473.

47. Sasaki, T.; Ukyo, Y.; Kuroda, K.; Arai, S.; Muto, S.; Saka, H., Crystal Structure of $Ce_2Zr_2O_7$ and β-$Ce_2Zr_2O_{7.5}$. *J. Ceram. Soc. Jpn.* **2004**, *112*, 440-444.

48. Schuck, G.; Kazakov, S. M.; Rogacki, K.; Zhigadlo, N. D.; Karpinski, J., Crystal Growth, Structure, and Superconducting Properties of the β-Pyrochlore KOs_2O_6. *Phys. Rev. B* **2006**, *73*, 144506.

49. Norberg, S. T.; Tucker, M. G.; Hull, S., Bond Valence Sum: A New Soft Chemical Constraint for *RMCProfile*. *J. Appl. Crystallogr.* **2009**, *42*, 179-184.

50. Shoemaker, D. P.; Seshadri, R.; Hector, A. L.; Llobet, A.; Proffen, T.; Fennie, C. J., Atomic Displacements in the Charge Ice Pyrochlore $Bi_2Ti_2O_6O'$Studied by Neutron Total Scattering. *Phys. Rev. B* **2010**, *81*, 144113.

Figures

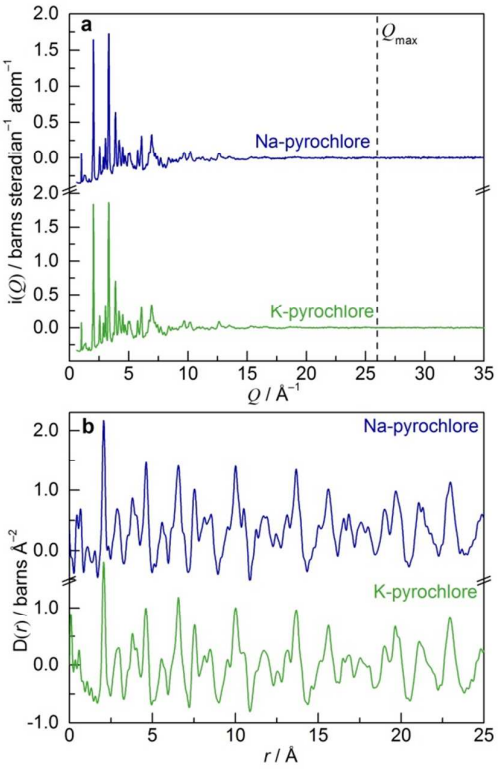

Figure 1: Distinct scattering functions, i(Q), for Na- (blue) and K-pyrochlores (green) produced through merging Bragg scattering data from four detector banks on GEM (banks 2-5) are shown in a). The dashed line illustrates the selection of Q_{max} = 26 Å^{-1}. The use of this value with the step modification function in the Fourier transform (Equation 1) results in the pair distribution functions (PDFs) of the Na- (blue) and K- (green) pyrochlores plotted out to r = 25 Å.

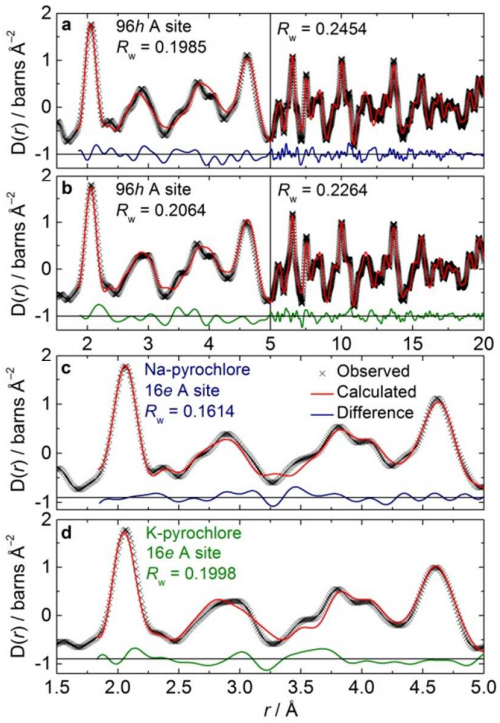

Figure 2: Least squares refinement of the Rietveld models ($Fd\bar{3}m$ 96*h* A site) against PDF data for the a) Na- and b) K-pyrochlores up to r = 20 Å. Separate fits and associated statistics to these are shown; the first up to 5 Å and the second from 5 to 20 Å. Panels c) and d) show fits to the low r region using the lower symmetry $F\bar{4}3m$ space group. Data are shown as black crosses, calculated PDFs as red lines, and difference curves as blue and green lines for the Na- and K-pyrochlores, respectively.

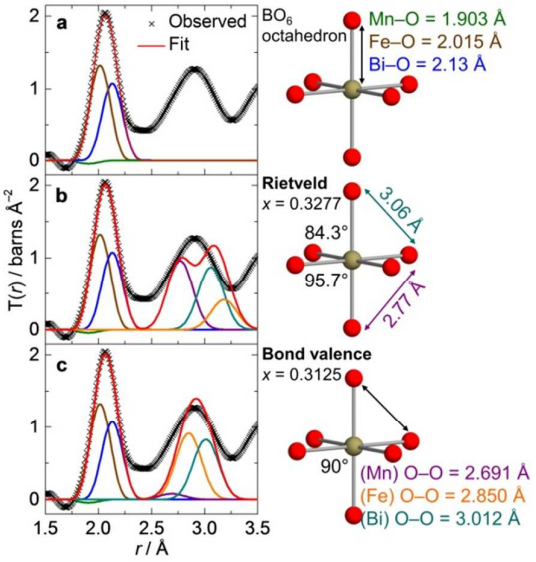

Figure 3: Fitting of the a) first correlation in T(r) of the Na-pyrochlore using partial contributions from B–O distances determined from bond valence. Atomic pair displacement parameters, which determine partial widths, were fixed to 0.0687 Å^2. Contributions of O–O atom pairs based on the average Rietveld model (O 48f x = 0.32770(7)) are shown in b) and those based around ideal BO_6 octahedra in c), respectively. Displacement parameters for O–O pairs were set to 0.1 Å^2.

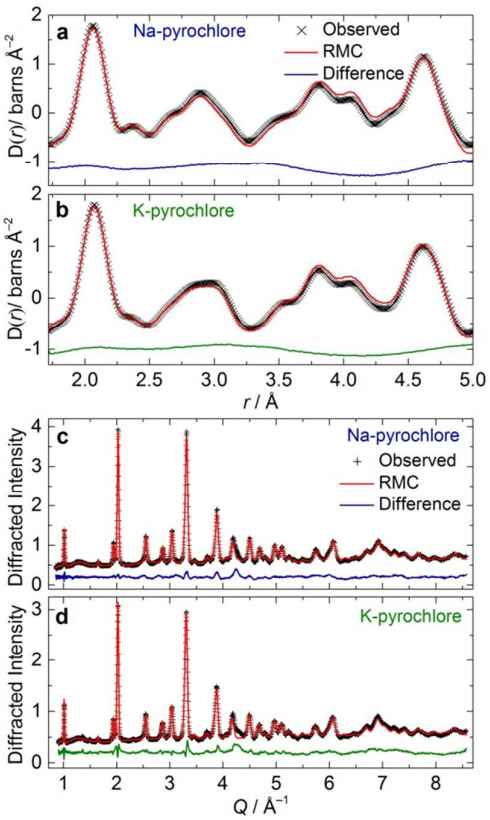

Figure 4: RMC fits to the D(*r*) and Bragg data of the a) and c) Na-pyrochlore, b) and d) K-pyrochlore, respectively. Data are shown as black crosses, fits as red lines, and difference curves as blue and green lines for the Na- and K-pyrochlores, respectively.

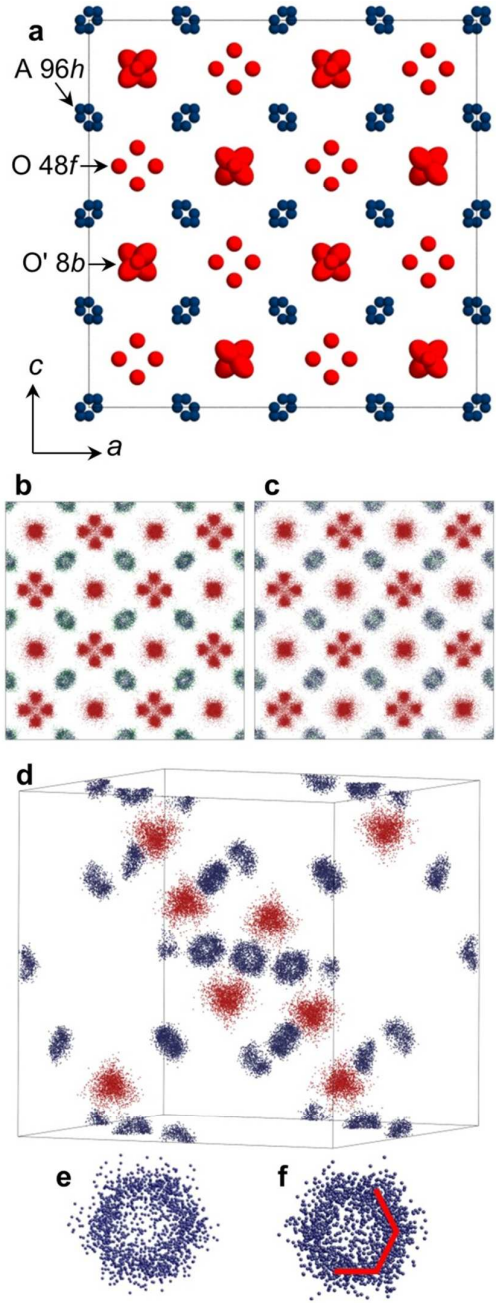

Figure 5: a) The refined crystal structure of $(Na_{0.60}Bi_{1.40})(Fe_{1.06}Mn_{0.17}Bi_{0.77})O_{6.87}$ from Rietveld analysis viewed along the [010] direction with B site atoms removed, highlighting displaced 96*h* positions used to model the A site cations. Final atomic arrangements from RMC supercells for Na- and K-pyrochlores are shown in b) and c), respectively. The majority of the disorder within these pyrochlores exists within the A_2O' network, as illustrated in d) for the K-pyrochlore where distributions of A and O′ sites both exhibit distinct shapes. Example A site Bi^{3+} distributions viewed along the [111] direction are shown for the e) Na- and f) K-pyrochlores displaying the formation of hollow tori. The red line represents the six-fold symmetry of these distributions and acts as a guide to the eye. Bismuth atoms are shown in blue, alkali metals in green, and oxygen in red. B site atoms are not shown.

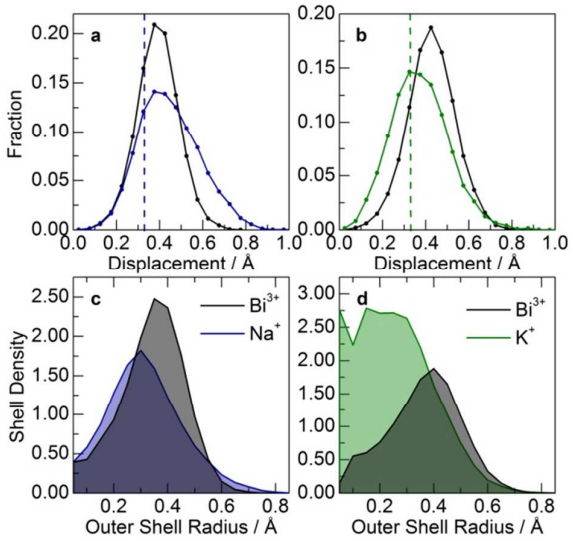

Figure 6: Histograms of cation displacement away from the ideal 16*d* crystallographic position for the A site metals in the a) Na- and b) K-pyrochlores. Histograms of shell density display cation distributions as a function of distance from the ideal position in c) and d) for the Na- and K-pyrochlore, respectively (shells are concentric hollow spheres increasing in radius from the ideal position). Densities for bismuth and sodium are highest close to average displacements, supporting the observation of hollow tori through supercell visualisation, whereas potassium is uniformly distributed within flattened ellipsoids.

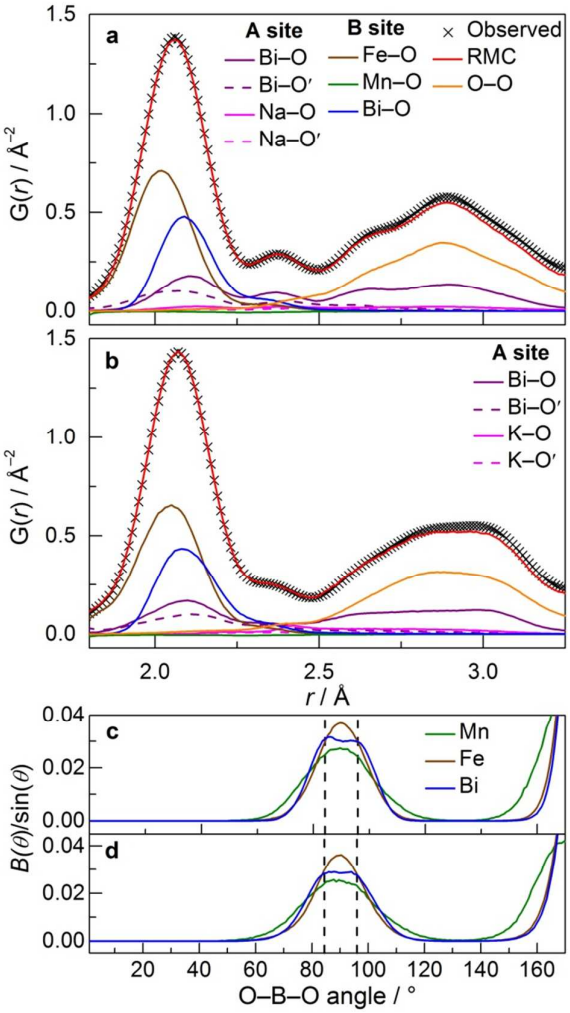

Figure 7: Partial PDFs for a) Na- and b) K-pyrochlores displaying contributions from nearest neighbour correlations involving the A and B sites and their local oxide ions, as well as the shortest oxygen-oxygen distance also. Comparison of O–B–O (where B = Fe^{3+}, Mn^{4+} and Bi^{5+}) bond angle distributions for the c) Na- and d) K-pyrochlores. dashed lines represent angles from the Rietveld models (approximately 85/95° in both pyrochlores) which give an average picture of the environments local to the three separate B site metals. The partials and bond angle distributions were calculated from 100 refined configurations that were summed together.

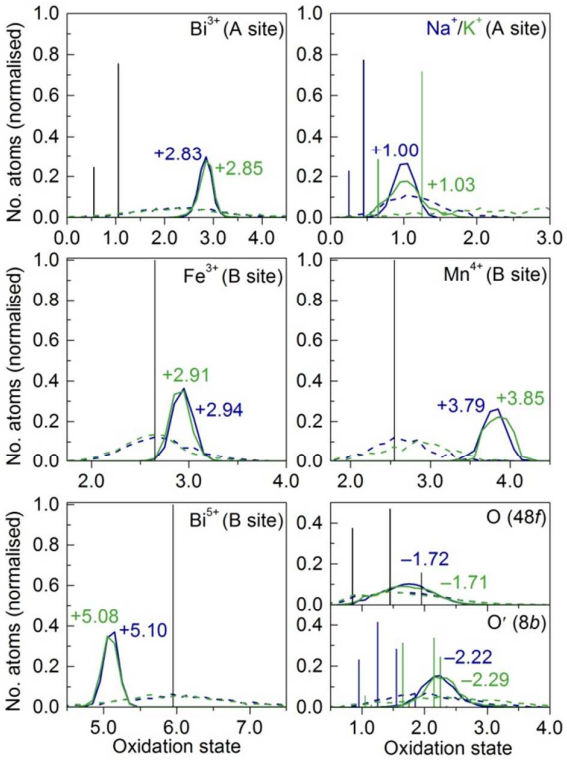

Figure 8: Bond valence distributions from RMC modelling for each atom type in the Na- (blue) and K-pyrochlores (green). Initial (Rietveld) values are shown as delta functions. Distributions from configurations using bond valence (BV) constraints are shown as solid lines, while distributions from configurations without BV constraints are shown as dashed lines. Oxidation states shown on the plots are average values from configurations using BV constraints.

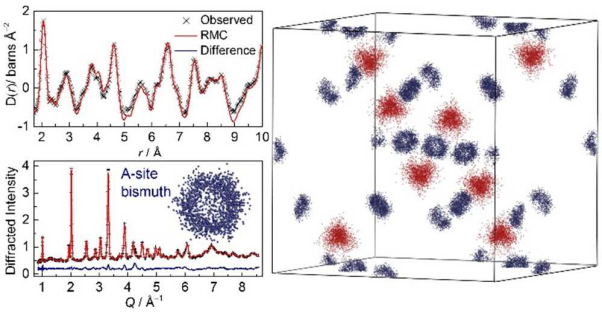

Table of Contents Graphic

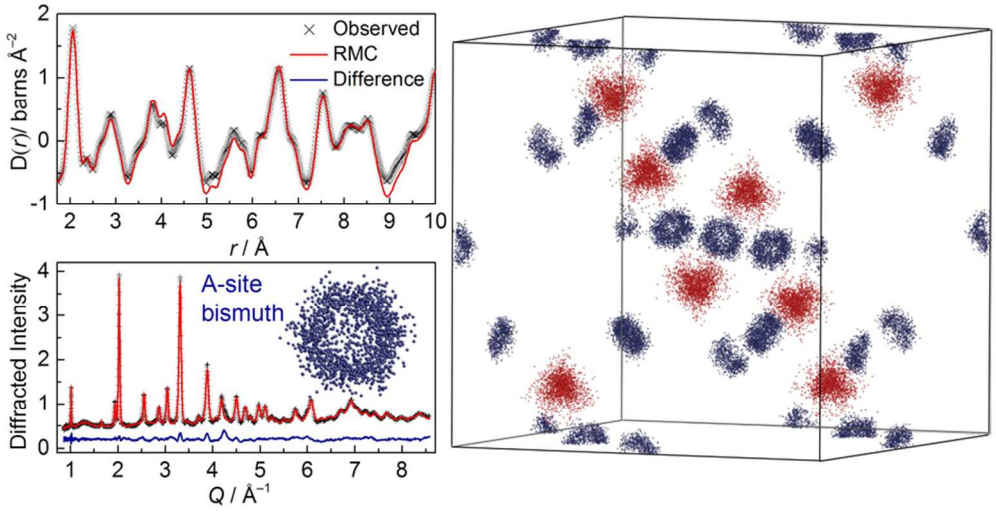

42x21mm (600 x 600 DPI)

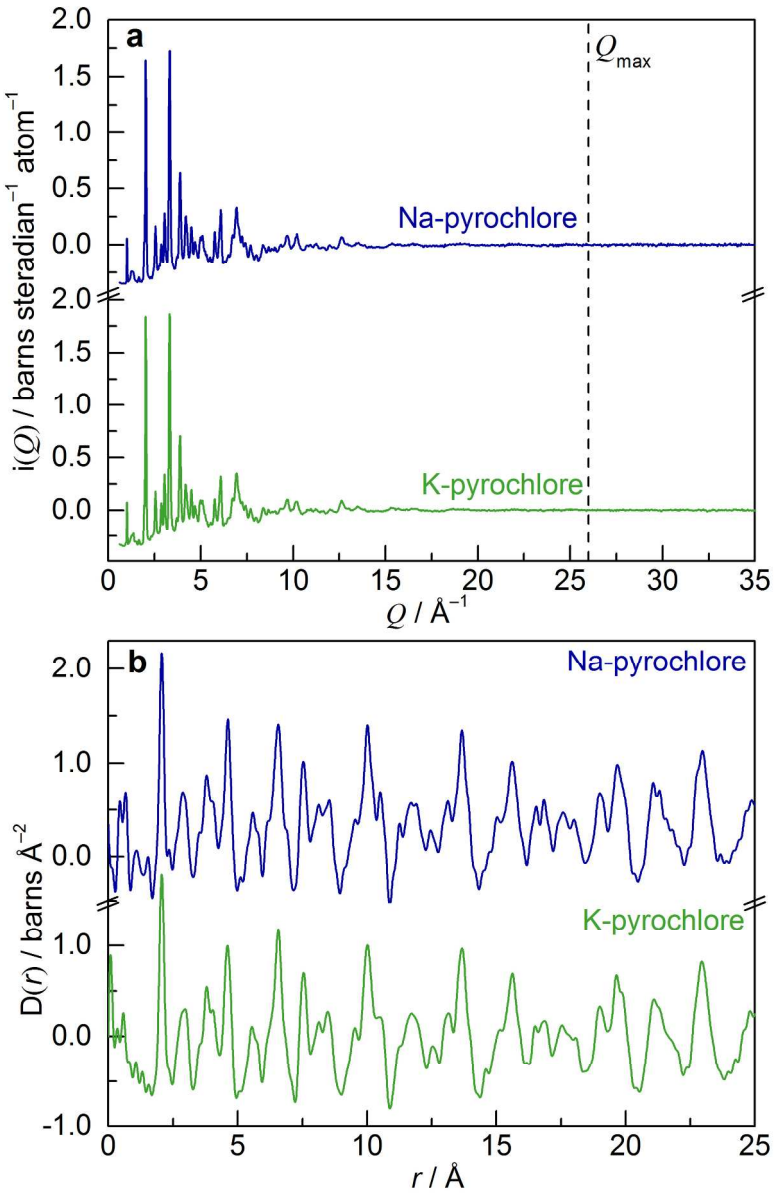

229x353mm (300 x 300 DPI)

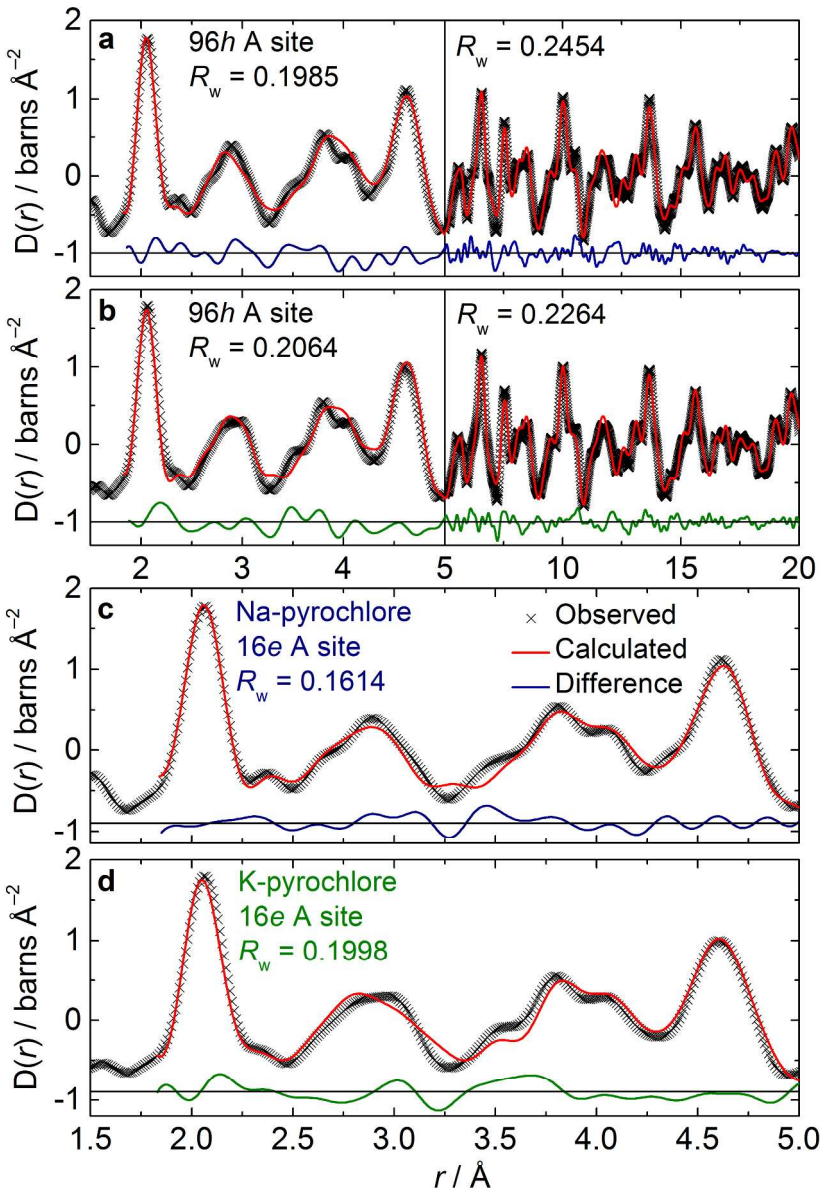

276x403mm (300 x 300 DPI)

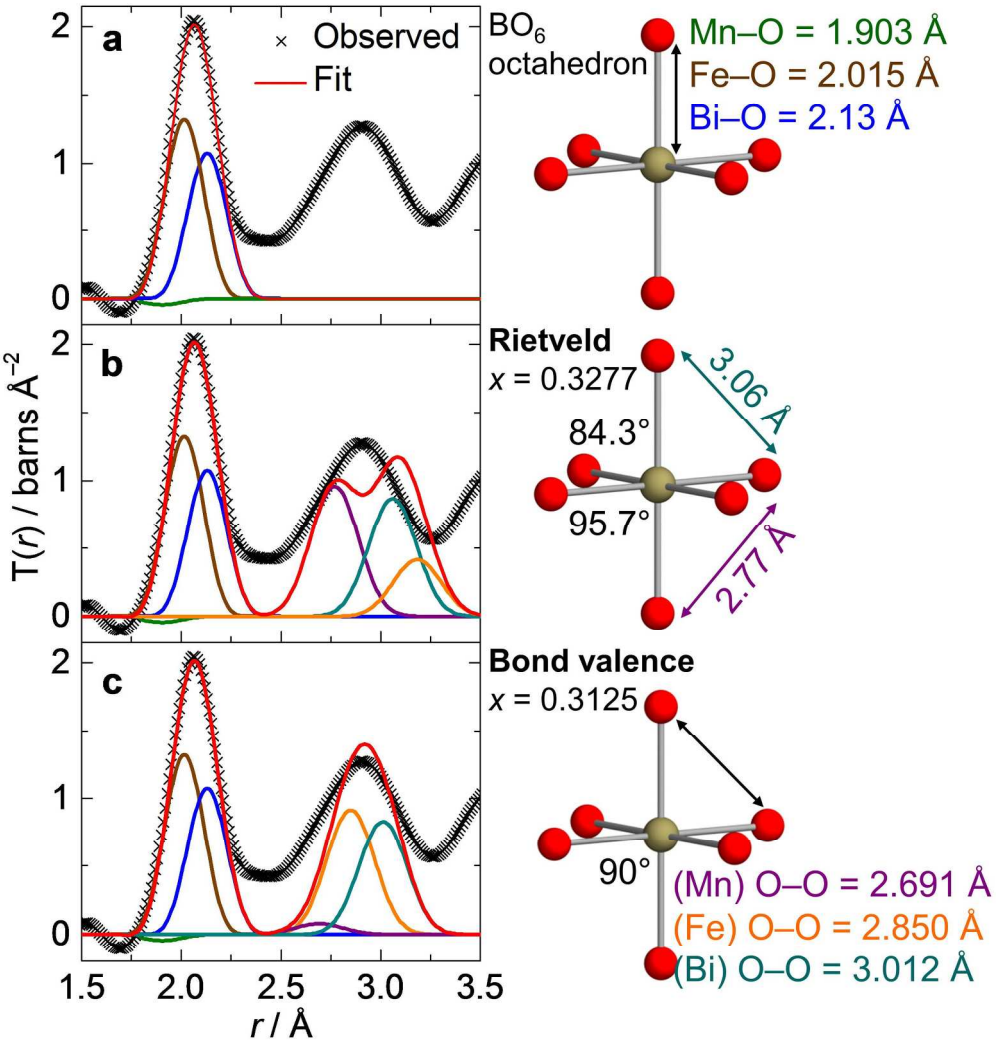

209x220mm (300 x 300 DPI)

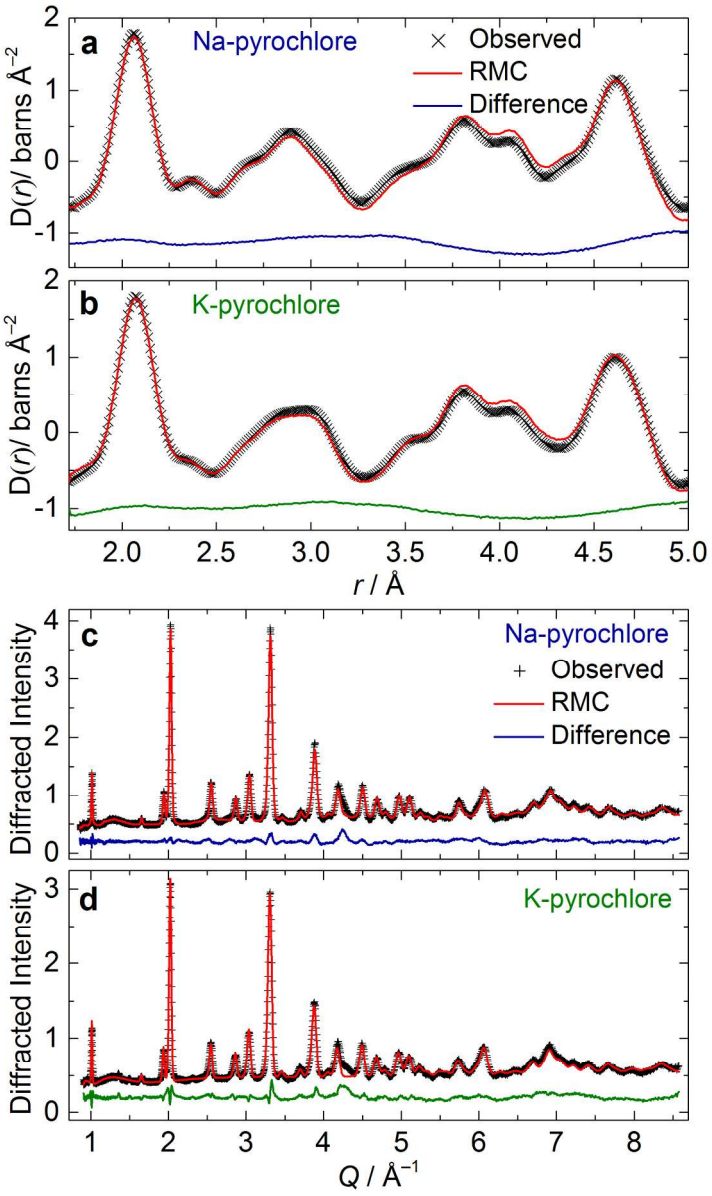

194x324mm (300 x 300 DPI)

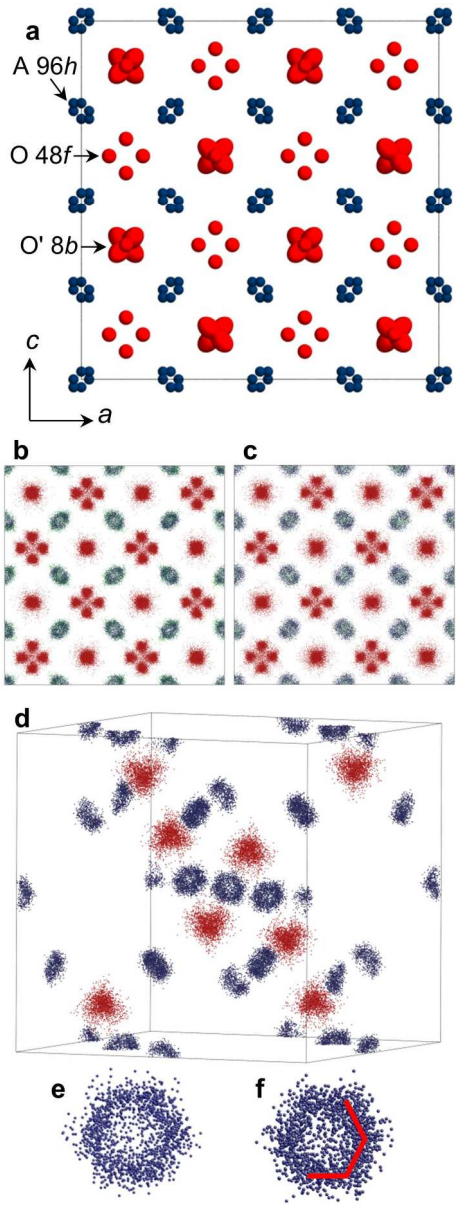

187x491mm (300 x 300 DPI)

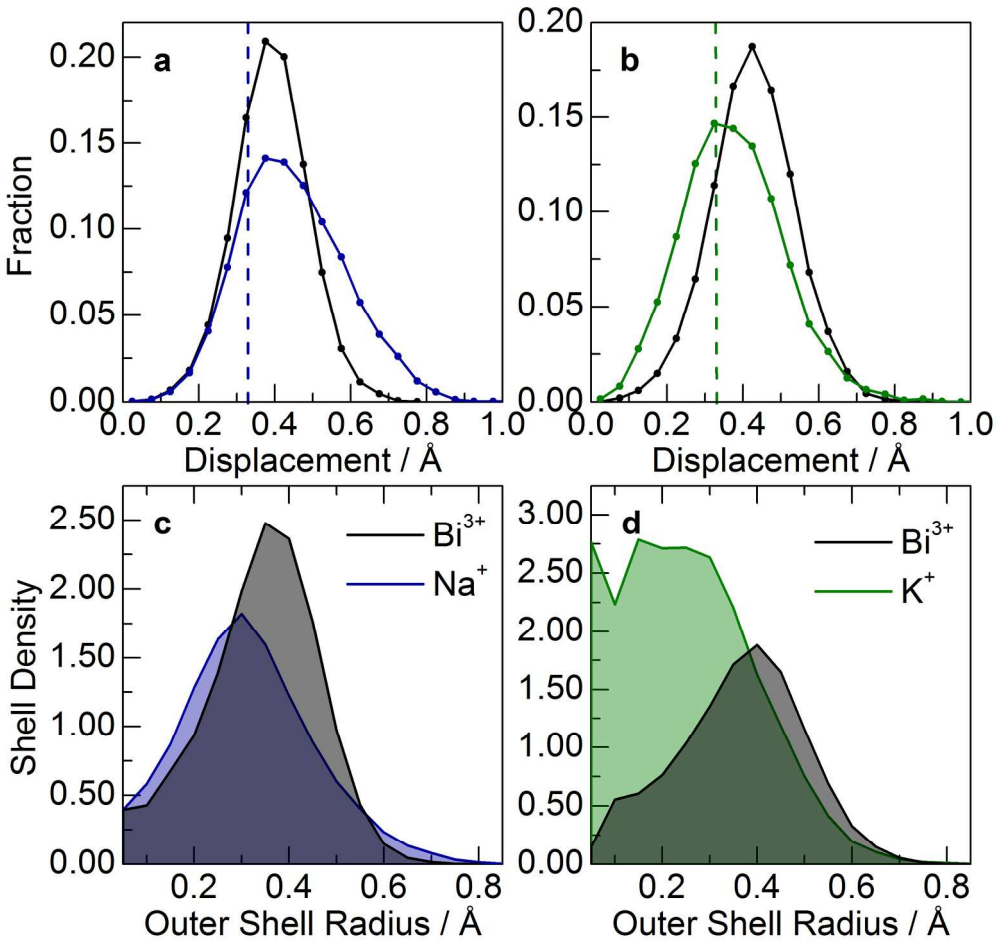

200x190mm (300 x 300 DPI)

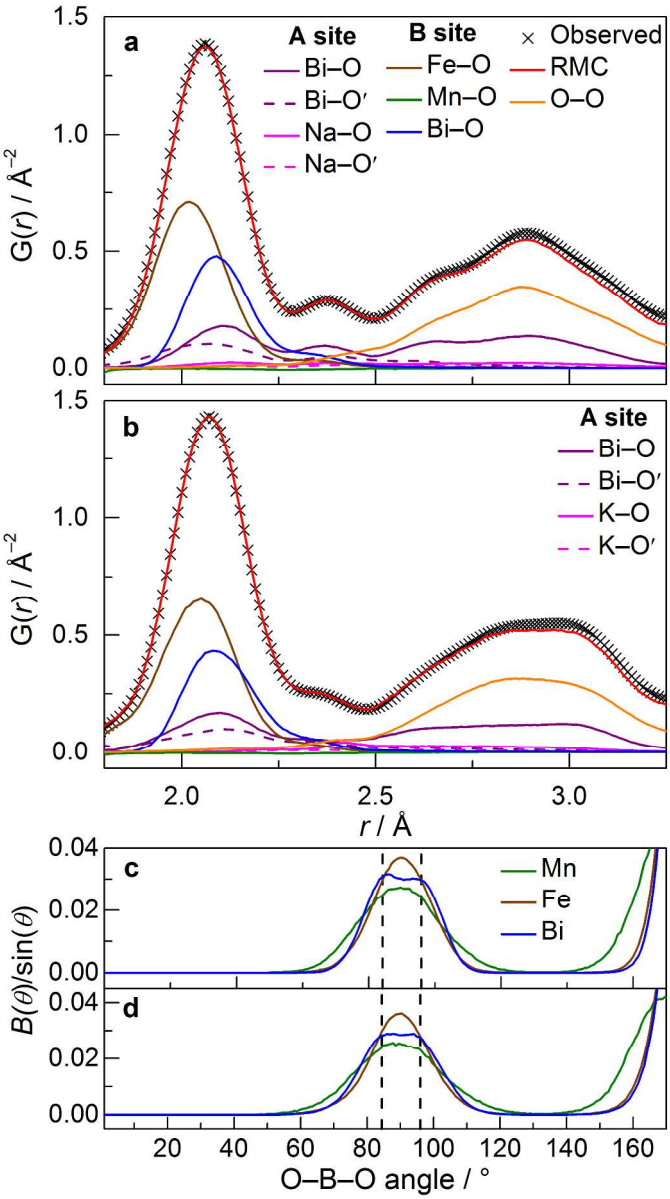

298x533mm (300 x 300 DPI)

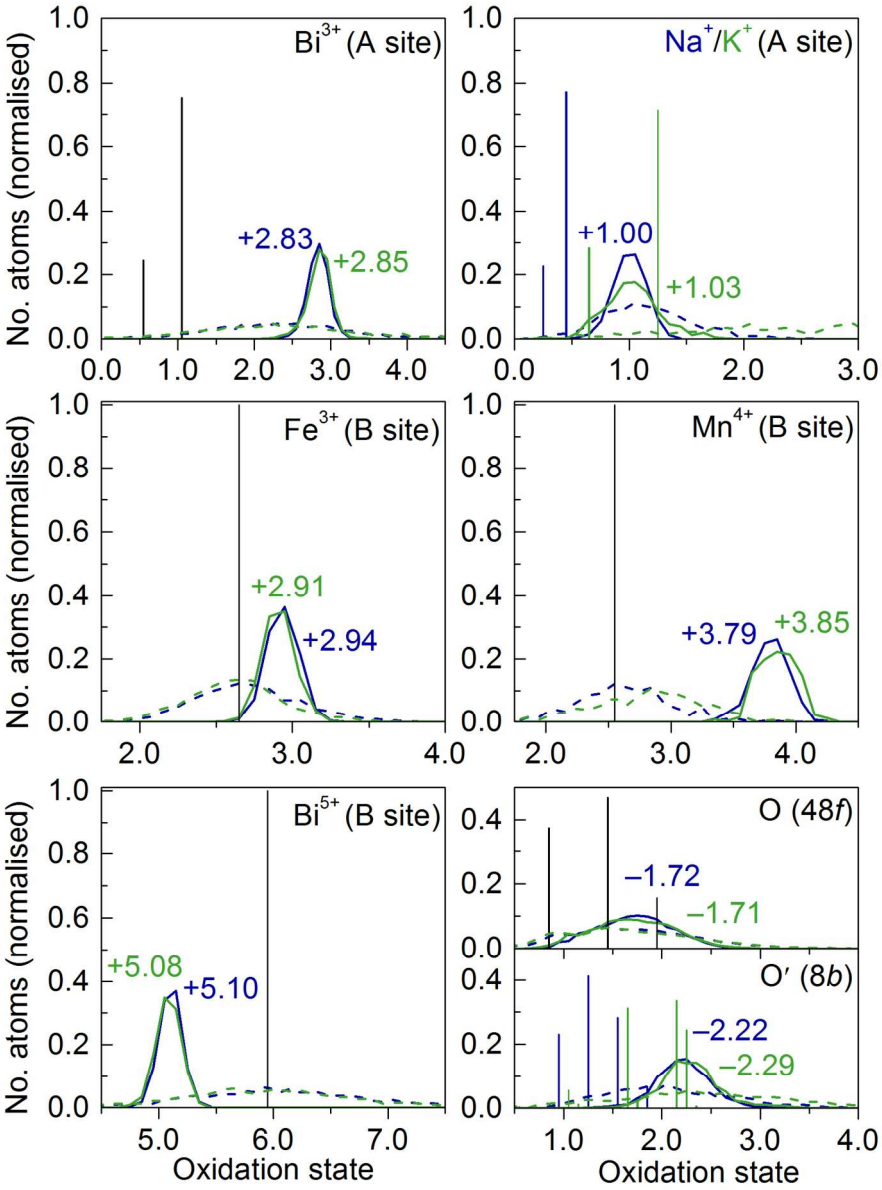

160x215mm (300 x 300 DPI)